



Flame-acoustic response measurements in a high-pressure, 42-injector, cryogenic rocket thrust chamber

Wolfgang Armbruster^{a,*}, Justin S. Hardi^a, Michael Oschwald^{a,b}

^a DLR, Institute of Space Propulsion, Im langen Grund, Hardthausen 74239, Germany

^b RWTH Aachen University, Institute of Jet Propulsion and Turbomachinery, Templergraben 55, Aachen 52062, Germany

Received 6 November 2019; accepted 15 May 2020

Available online xxx

Abstract

This work presents measurements of acoustically driven flame dynamics in a 42-element, cryogenic oxygen-hydrogen rocket thrust chamber under supercritical injection conditions. The experiment shows self-excited combustion instabilities for certain operating conditions, and this work describes the nature of the flame dynamics driving the acoustic field, as far as it can be ascertained from state-of-the-art optical measurements. Optical access has been realized in the combustion chamber with both fibre-optical probes and a viewing window. The probes collect point-like measurements of filtered OH* radiation. Their signals were used to calculate the gain and phase of intensity oscillations with respect to acoustic pressure for both stable and unstable operating conditions. Through the window, synchronized high-speed imaging of the flame in filtered OH* and blue radiation wavelengths was collected. The 2D flame response was related to the local acoustic pressure to investigate the distributed intensity and phase relationships. The flame response from OH* measurements is in agreement with the theory of Rayleigh. For stable conditions the oscillations of combustion and pressure were out of phase, whereas for an excited chamber 1T mode the oscillations were closely in phase. The integrated Rayleigh index from blue imaging was not consistent with the OH* results. The reason lies in the depth of field captured by this type of imaging, and must be used in a complementary fashion together with OH* imaging. The flame response values and 2D visualization presented in this work are expected to be of value for the validation of numerical modelling of combustion instabilities.

© 2020 The Author(s). Published by Elsevier Inc. on behalf of The Combustion Institute.

This is an open access article under the CC BY license. (<http://creativecommons.org/licenses/by/4.0/>)

Keywords: Combustion instabilities; Liquid propellant rocket engines; Flame visualization; Transcritical injection

1. Introduction

A large risk for liquid-propellant rocket engines (LPREs) is the occurrence of high-frequency combustion instabilities [1]. The theoretical principal of

* Corresponding author.

E-mail address: Wolfgang.Armbruster@dlr.de (W. Armbruster).

<https://doi.org/10.1016/j.proci.2020.05.020>

1540-7489 © 2020 The Author(s). Published by Elsevier Inc. on behalf of The Combustion Institute. This is an open access article under the CC BY license. (<http://creativecommons.org/licenses/by/4.0/>)

thermoacoustic driving that leads to the dangerous combustion instabilities is known as the Rayleigh criterion [2]. A mathematical description of the Rayleigh criterion is given in Eq. (1) and describes that the condition for amplitude growth is fulfilled if heat release rate oscillations (\dot{q}') are in phase with pressure oscillations (p').

$$\int_0^T \int_V p'(x, t) \dot{q}'(x, t) dV dt > 0 \quad (1)$$

For that reason, it is important to gain a detailed understanding of the interaction of combustion chamber acoustics and combustion.

While the chamber acoustics are theoretically well understood, it is crucial to properly describe the flame response to the pressure or mass flow oscillations in order to be able to predict unstable combustion. Functions describing the frequency dependent flame response are referred to as flame transfer functions (FTF) and are usually defined as normalized integrated heat release rate oscillations \bar{Q}' in response to acoustic velocity (u') [3–7] or p' [8–10], as given in Eq. (2). However, in this study the focus is confined to the flame response at the main instability frequency.

$$FTF(\omega) = \frac{\bar{Q}' / \bar{Q}}{p' / \bar{p}} \quad (2)$$

Heat release rate cannot be measured directly. For LPRE combustion, high-speed OH* radiation imaging has been used as a marker for heat release rate to study acoustic-flame interaction [8,11,12]. However, Fiala et al. [13,14] found that OH* radiation suffers from self-absorption at pressures found in LPREs. The images are dominated by emission from the reaction zone surface closest to the observer [14]. Furthermore, at temperatures above 2700 K [14], this emission is dominated by thermal excitation of OH* rather than chemiluminescence. Its connection with \dot{q}' is therefore not straightforward. Fiala et al. also investigated radiation in the blue region of the O₂-H₂ spectrum [13,14]. Blue radiation does not suffer from self-absorption and provides a greater depth of field than OH*. Unfortunately, there is no established proportionality between line-of-sight integrated radiation measurements and \dot{q}' , neither for blue nor OH* wavelengths [13]. On the other hand, measured flame radiation dynamics can be used as validation data for combustion modelling and FTFs can be extracted from the simulations. However, such measurements under conditions relevant for LPREs are exceedingly rare.

To address this lack of experimental data, optical access in the form of fibre-optical probes and a small viewing window has been realized in a sub-scale, experimental rocket thrust chamber, designated 'BKD' [15]. BKD operates with liquid oxygen (LOX) and H₂ at power density levels ranging from 30 to 70 GW/m³, which is highly representa-

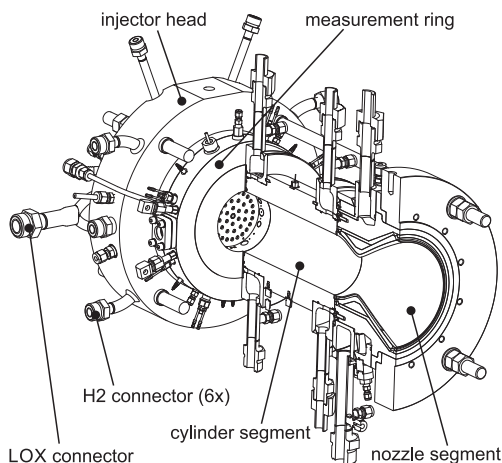


Fig. 1. DLR research combustor BKD.

tive of European engines and exhibits self-excited combustion instabilities of the injection-coupled type for certain operating conditions [16]. Therefore, BKD is able to fill the gap between other lab-scale combustion instability experiments and expensive full-scale engine tests.

BKD became a well-known modelling test case based on its combustion stability as characterized by p' measurements [9,10,17,18]. The present work aims to increase the utility of the test case by extending the data base with optical flame response measurements. First, the dependence of radiation oscillation intensity and phase from the point-like optical probe measurements on p' for various operating conditions will be established. The analysis is confined to the frequency of the main acoustic mode of instability, the first tangential (1T) mode around 10 kHz. Rayleigh indices calculated according to Eq. (2) are consistent with combustor stability. Then, the distributed flame response will be assessed from synchronous OH* and blue radiation imaging. The different types of imaging provide complementary information on flame phenomenology, but only the OH* gives integrated flame response values consistent with a Rayleigh source.

2. Experimental setup

2.1. Combustor BKD

The experiments were performed with the DLR research combustor model 'D' (BKD). BKD, as shown in Fig. 1, has a conventional LPRE setup with an injector head, a 200-mm long cylindrical chamber segment, and a convergent-divergent nozzle. The combustion chamber diameter is 80 mm and the contraction ratio of the nozzle is 2.56. The injector consists of 42 shear coaxial elements. The

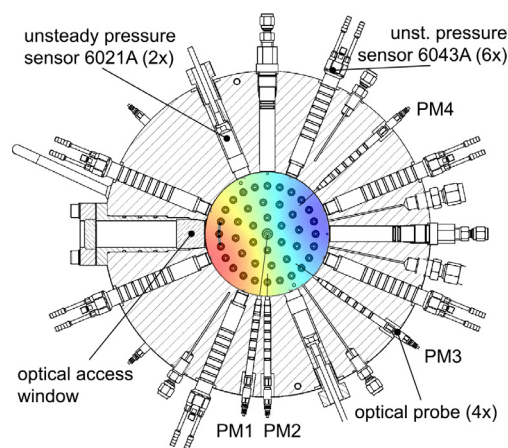


Fig. 2. Current version of the measurement ring with optical access window. An interpolated 1T pressure field is also indicated.

LOX posts are 68 mm long and have a inner diameter of 3.6 mm. Their outlet is tapered and recessed by 2 mm.

An instrumented 'measurement ring' is placed between the injector head and the combustion chamber. An earlier version developed by Grning et al. [19] included eight circumferentially distributed unsteady pressure sensors and three fibre-optical probes (probes A, B and C). The measurement plane of the sensors in the ring is 5.5 mm downstream of the injection plane. The pressure sensors have a measurement range of ± 30 bar and the signals are sampled with 100 kHz.

Following positive experience with the fibre-optical probes, a new version of the measurement ring was developed which features an optical access window enabling 2D visualization of one of the flames in the outer row of injectors, as shown in Fig. 2. A local protective film of ambient temperature H_2 injected through a slot spanning the window to shield it from the hot gases. The new ring contains eight flush-mounted pressure sensors and four optical probes in the same plane. This paper will present analysis of measurements from both versions of the measurement ring. All the 2D images were made using the new measurement ring, while all the measurements of the three optical probes A, B and C were obtained using the measurement ring described in [19].

2.2. Optical diagnostics

The optical probes contain a small sapphire rod through which the radiation is first transferred to optical fibres and then transported to photomultipliers (PMs). 310 ± 5 nm OH^* filters are installed between the fibres and the PM detectors. The intensity signals $I(t)$ are sampled with 100 kHz. The full

Table 1
Operating conditions of the load points.

	LP1	LP2	LP4	LP5	LP6
p_{cc} [bar]	70	69.9	80.7	81.7	77.8
ROF [-]	3.9	5.9	5.9	4.8	5.2
T_H [K]	94	95	95	103	102
T_O [K]	111	111	111	113	115
J [-]	34	15	14	24	21
$p'_{1T,p-p}$ [%]	2.1	5.3	15.6	4.5	2.2

acceptance angle of the optical probes is less than 2° [19]. The narrow field of view of the probes is used to align each probe with individual flames of the outer ring of the injector pattern, as indicated in Fig. 2. The position and injector alignment of the first measurement ring can be found in [19].

The optical access window could be realized with an 18-mm diameter. The window is aligned with one of the outer ring injectors. Due to a slight overlap of the window with the faceplate, the first 17.5 mm, or about five LOX injector diameters of the flame can be observed. CFD simulations of BKD indicate that about 50% of the total Rayleigh index is contained within the extent of the window [17]. High-speed imaging of OH^* (310 ± 5 nm) and blue (436 ± 5 nm) radiation was realized with two synchronized cameras at 60,000 frames per second (FPS). More details of the optical setup can be found in Ref. [15].

2.3. Operating conditions

The steady-state operating conditions, or load points (LPs), analyzed in this work are defined by the static combustion chamber pressure p_{cc} and the propellant mixture ratio ($ROF = \dot{m}_O / \dot{m}_H$). The upper limit of the operating range of BKD is the LP 80 bar and ROF 6.8, which has a thermal power of about 90 MW and thrust of 24 kN, placing its performance at the lower end of the scale of upper stage engines.

In this study five different LPs with total mass flow rates ranging from 5.5 to 6.7 kg/s were investigated. The operating and injection conditions, such as the propellant injection temperatures T_H and T_O , and the injection momentum flux ratio $J = (\rho u^2)_H / (\rho u^2)_O$ of each LP are summarized in Table 1. Furthermore, maximum peak-to-peak (p-p) amplitudes of 1T filtered p' signals ($p'_{1T,p-p}$) for each LP, indicating stable and unstable conditions, are also given in the table. The first three load points (LP1-LP4) are labelled according to the LPs in test cases HF-7 and HF-9 of the French-German Rocket Engine Stability initiative (REST).

The five LPs, show different stability characteristics, as the $p'_{1T,p-p}$ values indicate. LP1 and LP6 can be considered as stable. Figure 3 shows the acoustic spectra of the combustion chamber in form of a PSD averaged over all eight sensors for

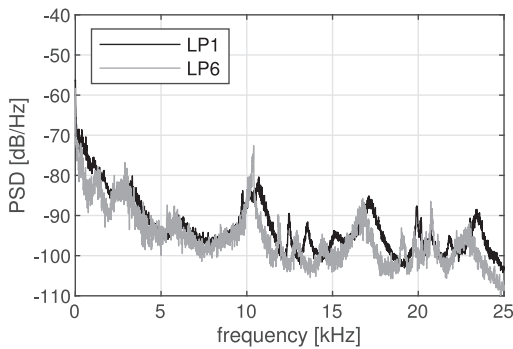


Fig. 3. PSDs of chamber pressure oscillations for stable conditions.

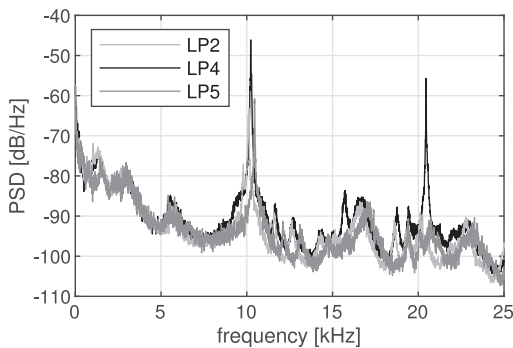


Fig. 4. PSDs of chamber pressure oscillations for load points with an excited 1T mode at about 10 kHz.

stable combustion. The reference pressure for the dB-scale is the mean chamber pressure p_{cc} .

In comparison, Fig. 4 shows PSDs for the other three load points (LP2, LP4, LP5). An excitation of the chamber 1T mode at about 10 kHz can now clearly be observed. LP4 shows the largest amplitudes and therefore the highest 1T peak in the PSD. In addition, a non-linear overtone can be detected at about 20.5 kHz for LP4. The load points LP2 and LP5 show a similar excitation of the 1T mode, but with a lower peak height.

3. Methodology

3.1. Analysis of optical probe signals

Previous work showed that the main instability in BKD appears at about 10 kHz. At that frequency the flames are modulated by resonance of the second longitudinal mode (2L) of the LOX posts and this fluctuation can in turn excite the 1T mode in the combustion chamber [16]. The analysis in this article will therefore focus on the flame response to the 1T mode, filtered to this frequency range.

The signal I' from each optical probe is compared with p' from the closest pressure sensor to the probe location. This simplification leads to a maximum error in 1T amplitude of 8 %. The phase of p' at the probe location has an error of less than 11° for spinning 1T modes and 0° for standing 1T modes.

The p' and I' signals are first band-pass filtered with a 2nd order Butterworth filter without phase shift. The filtered $p'(t)$ and $I'(t)$ signals can be taken as monofrequent. Analytic signals created with the Hilbert transform were used to calculate the instantaneous phase $\phi(t)$ and amplitudes $\hat{p}(t)$ and $\hat{I}(t)$ of both signals. The normalized gain n of the flame response is calculated with Eq. (3).

$$n = \frac{\hat{I}'/\bar{I}}{\hat{p}'/p_{cc}} \quad (3)$$

The phase difference between the two signals can be interpreted as the phase of the flame response at that frequency, as shown in Eq. (4).

$$\Delta\phi = \phi_{p'} - \phi_{I'} \quad (4)$$

3.2. Analysis of 2D flame visualization

The high-speed imaging was analyzed using the multi-variable Dynamic Mode Decomposition (DMD) approach following Beinke [8]. The unsteady pressure sensor signals are resampled to the time vector of the series of images from the cameras and handled as additional pixels in a DMD analysis. The DMD is performed to isolate the flame radiation dynamics at certain frequencies, in this case selecting the DMD mode corresponding to the peak response near 10 kHz. After processing the DMD, the pseudo-pixels containing the pressure sensor signals are separated from the spatial mode matrix of the DMD results before both data types are reconstructed separately. With this method it is possible to compare flame dynamic modes and pressure oscillations at the same frequency, with the phase relationship retained.

For a 2D flame response, it is necessary to have a pressure field distribution throughout the extent of the window. The acoustic pressure field in the plane of the pressure sensors is reconstructed using a simple spline-interpolation method between p' signals at all eight sensor locations and with the additional assumption of zero pressure gradient normal to the wall. An exemplary interpolated 1T pressure field in the plane of the measurement ring is shown in Fig. 2 with the dominant orientation for LP4. It can be assumed that the longitudinal distribution of the 1T amplitude is constant within the extent of the optical access window [9,10]. By combining the information of the pressure field in the area of the window and the flame radiation dynamics, it is possible to calculate a 2D Rayleigh-Index for a selected DMD mode with Eq. (5), where $\theta_{p'}$ is the phase of each pixel calculated via DMD and $\theta_{I'}$ is the phase

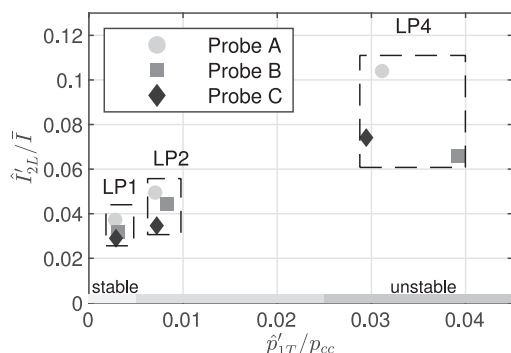


Fig. 5. Magnitude of flame response for LP1-LP4 at the main coupling frequency of 10 kHz.

of the pressure oscillation in the window location calculated by the described pressure field interpolation method.

$$RI(x, y) = |I'(x, y)| |p'(x, y)| \cos(\theta_{I'}(x, y) - \theta_{p'}(x, y)) \quad (5)$$

4. Results

4.1. Flame response from optical probes

First, the flame response of the first three LPs, each 1 s long, using the optical probes is presented. Fig. 5 shows the filtered and normalized RMS amplitude of the OH* oscillation plotted over the acoustic pressure RMS amplitudes. The abscissa also shows the stability classification of Gröning [20]. According to this scale, LP1 is a stable load point and LP4 is unstable. LP2 is in an intermediate zone, which Gröning defined as semi-unstable. As to be expected, the flames show a higher level of oscillation for more unstable load points.

In order to increase the resolution of the relationship between flame response and pressure, the signals from the full length of a single test run were analyzed. The test including 10 different operating conditions was cut into 0.2 s time windows. Fig. 6 shows the response magnitude for the three optical probes of the first measurement ring over a complete test run. It can be seen that the flame response is not linear. For higher perturbation amplitudes the gain n , decreases. Similar observations have been reported by Boudy et al. [3]. Power law curves have been fitted to the set of points from each of the optical probes. The coefficient of determination (R^2) values of the fits were between 0.9 and 0.95 and the exponent is consistently around 0.36.

The procedure for processing the optical probe data described in Section 3.1 produces a time series of phase difference ($\Delta\phi(t)$). This phase difference is

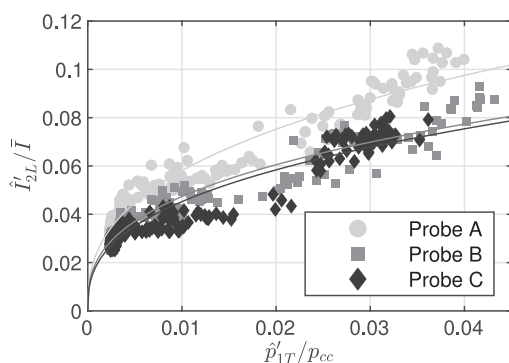


Fig. 6. Magnitude of flame response over a full run for the main coupling frequency of 10 kHz.

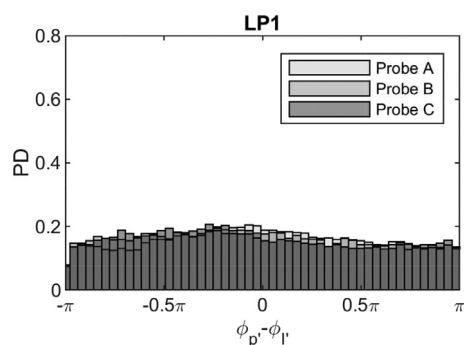


Fig. 7. Phase difference between p' and I' for three optical probe locations during LP1 (stable).

not constant, and so it is best analyzed statistically. Here, we present the results as probability distributions following Gröning [19,20], but with improved resolution.

Fig. 7 shows the probability distribution of the phase shift for the stable LP1. The distribution of 100,000 samples is close to homogeneous. This is consistent with the previous observation of Gröning et al. for stable combustion and was explained by diverging frequencies of the LOX post and combustion chamber resonances [19]. In terms of the Rayleigh criterion, this result can be interpreted as an equal ratio of periods with driving and damping, and the net energy transfer into the chamber 1T mode is close to zero.

In comparison, Fig. 8 shows the probability distribution of the phase difference for the unstable LP4. In this case a clear tendency towards a single phase difference can be observed. The phase shift with the highest probability lies between -0.3π and $+0.1\pi$. This means that at all three optical probe locations, energy can be transferred from combustion into the acoustic field, which is consistent with the excited 1T mode for this LP. Similarly, the semi-unstable LP2 (not shown here) has a tendency to

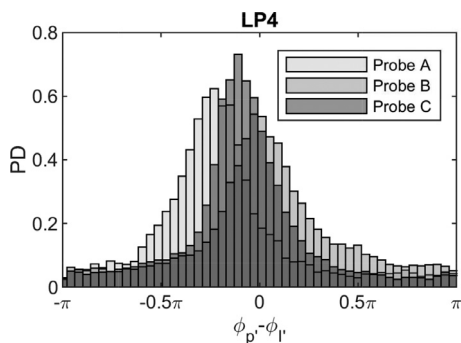


Fig. 8. Phase difference between p' and l' for three optical probe locations during LP4 (unstable).

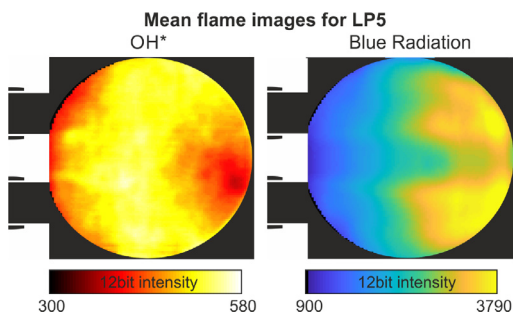


Fig. 9. Time-averaged OH* (left) and blue radiation (right) images of LP5 (semi-unstable). Adjusted from [15].

Table 2
Estimated n and τ values for the three LPs.

	LP1	LP2	LP4
$n [-]$	11.3 ± 1.9	5.7 ± 1.1	2.5 ± 0.7
$\tau [\mu s]$	–	–	-3.8 ± 5.5

wards a phase shift between -0.1π and $+0.4\pi$, although less pronounced than for LP4.

It is possible to estimate n and time lag τ values from the given investigation. The resulting values are presented in Table 2. Due to the very low pressure oscillation amplitudes, the highest n values are calculated with Eq. (3) for LP1 and LP2. However, a statistically significant phase shift can only be observed for LP4, which explains why this LP is the most unstable. The time lag corresponding to the measured time shift can be estimated by Eq. (6).

$$\tau = \frac{\Delta\phi}{2\pi f} \quad (6)$$

4.2. Flame visualization

The load points LP5 and LP6 are from tests with the optical access window. Time-averaged over 0.1 s OH* and blue radiation images for LP5 can be found in Figs. 9 and 10 for LP6, respectively.

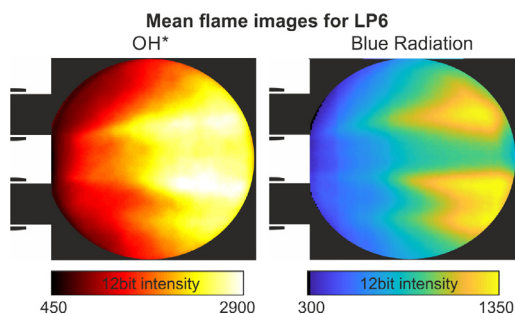


Fig. 10. Time-averaged OH* (left) and blue radiation (right) images of LP6 (stable).

Due to the strong self-absorption of OH*, one can mainly see the outer surface of the combustion zone in the mean OH* images in Figs. 9 and 10. The reason for the region with less intensity at the downstream end of the OH* image in Fig. 9 is currently unclear. However, in Fig. 10 the OH* mean image has a better quality and the flame topology can clearly be observed. The intensity field quickly becomes more uniform progressing downstream. In the blue images in Figs. 9 and 10, the darker core delineating the LOX jet can be seen, because it absorbs emission from the combustion zone behind it. Thus, the integrated line-of-sight intensity from the shear layers either side of the LOX core is far greater from the foreground in front of the core.

The two images provide complementary information on the flame phenomenology. The thin shear layer can be seen extending from the injection plane in both images. The path of the LOX core can be followed in the blue image. The rapid spreading of the reaction zone can be well traced in the OH* image, and indicates that flame-flame interaction becomes relevant by about three injector diameters ($3 D_O$) downstream.

4.3. Flame response from visualization

The 2D Rayleigh-Index (RI) distribution is calculated as described in Section 3.2 for LPs 5 and 6. Fig. 11 shows the RI for the semi-unstable LP5. The RI from OH* imaging (left side of Fig. 11) is mostly positive and only shows some areas with neutral or slightly negative values which are located in the regions between neighboring flames. It shows that the flame as observed in OH* radiation intensity is coupling with local p' more or less uniformly.

The RI distribution from blue imaging (right side of Fig. 11) differs from the OH* result quite significantly. Integrated over the observable area, the RI is only weakly positive. Alternating vertical structures are visible on the LOX core. These 'ripples' are due to modulation of the injected LOX flow resulting from the excited 2L mode of the LOX posts. These structures are only visible in blue imaging, owing to the better depth of view. Within the

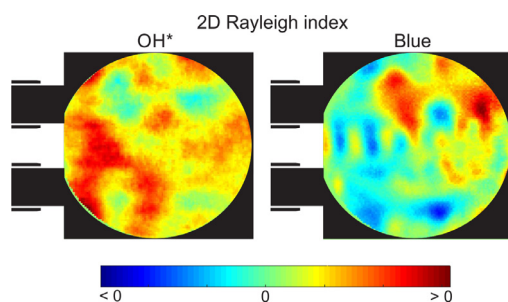


Fig. 11. 2D Rayleigh index distributions from OH* (left) and blue (right) imaging for LP5 (semi-unstable).

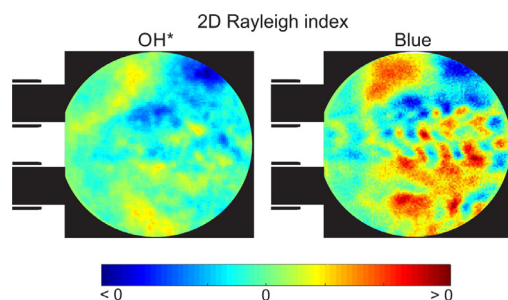


Fig. 12. 2D Rayleigh index distributions from OH* (left) and blue (right) imaging for LP6 (stable).

extent of the window, the ripples present as striations of alternating positive and negative RI, and very nearly cancel out in the area integration of the Rayleigh term.

An analytic model of shear-coaxial flame response by Nez et al. [21] predicts this kind of short wavelength pattern arising from eddy formation in the shear layer. The model showed that the integrated Rayleigh source term can still be positive due to the contribution from the end of the flame, which cannot be observed within the optical access window in BKD. The areas contributing positive RI in Fig. 11 correspond to the higher blue intensity regions either side of the LOX core further downstream, as seen in Fig. 9. This suggests that care should be taken in selecting an appropriate area for deriving RIs from blue imaging.

Fig. 12 shows the RI distributions in OH* and blue for the stable LP6. As to be expected, the integrated values are close to zero or slightly negative. The vertical striations on the LOX core are again visible in the blue result. Here, they are visible on the entire length of the LOX core because there is no coherent, in-phase I' fluctuation dominating the RI distribution like in the downstream half of the window in Fig. 11.

5. Conclusions

The flame response was investigated in an optically accessible, LOX/H₂ research rocket combustor with self-excited combustion instabilities. From previous work, the instability has peak amplitude around 10 kHz and is understood to arise from injection coupling. In this work, the dependence of fluctuating flame radiation amplitude and phase on acoustic pressure at the instability frequency was analyzed.

Relative amplitude and phase response of intensity oscillations could be established for a wide range of pressure amplitudes from point-like measurements of filtered OH* radiation via fibre-optical probes. A power law relation with an exponent of 0.36 was found to best describe the amplitude relationship. Probability density distributions of the phase difference between local intensity and pressure confirm the expected behavior of near in-phase coupling for unstable combustion and a lack of consistent phase for stable combustion.

The experiment also afforded a view of the first 18 mm of the flame through a small window. Simultaneous high-speed imaging in filtered OH* and blue wavelength ranges were captured for two operating conditions; one stable, one unstable. The two types of imaging provided complementary information on the flame topology. Under the assumption that the radiation intensity is a marker for heat release rate, the imaging was related to the local acoustic pressure and distributions of Rayleigh index were calculated. The integrated Rayleigh index from OH* imaging was consistent with the stability character and the optical probe measurements.

In the region of the LOX core the 2D RI showed alternating areas of driving and damping in longitudinal direction. Therefore the calculated 2D Rayleigh index images for blue radiation were not as consistent with stability characteristics as for RI from OH*. This was due to the greater depth of view of blue radiation and the interference of turbulent structures on the surface of the LOX core with line-of-sight integrated radiation intensity. This observation suggests that care should be taken in selecting an appropriate area for deriving RIs from blue imaging.

To the authors' knowledge, this study presents the first experimental flame response results at these representative conditions. It is expected that the 2D flame visualization as well as the flame response results represent valuable validation data for numerical simulations of combustion instabilities.

Declaration of Competing Interest

None.

Acknowledgments

Financial support has been provided by the German Research Foundation (DFG) in the framework of the SFB TRR40 Cooperative Research Centre. The work is also associated with the French-German Rocket Engine Stability initiative (REST). The authors would like to thank the crew of the P8 as well as Robert Stützer for setting up the optical diagnostics.

References

- [1] D. Harrje, F. Reardon (Eds.), *Liquid Propellant Rocket Combustion Instability*, NASA SP-194, 1972.
- [2] J.W.S. Rayleigh, *Nature* 18 (455) (1878) 319–321.
- [3] F. Boudy, D. Durox, T. Schuller, S. Candel, *Proc. Combust. Inst.* 33 (2011) 1121–1128.
- [4] M. Wierman, B. Pomeroy, W. Anderson, *Prog. Propuls. Phys.* 8 (2016) 55–74, doi:10.1051/eucass/201608055.
- [5] E. Freitag, *On the Measurement and Modelling of Flame Transfer Functions at Elevated Pressure*, TU München, München, Germany, 2009 Ph.D. thesis.
- [6] A. Kaufmann, F. Nicoud, F. Poinsot, *Combust. Flame* 131 (4) (2002) 371–385.
- [7] D. Durox, T. Schuller, N. Noiray, A.L. Birbaud, S. Candel, *Combust. Flame* 156 (2009) 106–1119.
- [8] S.K. Beinke, *Analyses of Flame Response to Acoustic Forcing in a Rocket Combustor*, School of Mechanical Engineering, The University of Adelaide, Australia, 2017 Ph.D. thesis. DOI: 10.25909/5b875ef6c13fb
- [9] M. Schulze, T. Sattelmayer, *Int. J. Spray Combust. Dyn.* 9 (4) (2017) 277–298, doi:10.1177/1756827717695281.
- [10] A. Urbano, Q. Douasbin, L. Selle, G. Staffelbach, B. Cuenot, T. Schmitt, S. Ducruix, S. Candel, *Proc. Combust. Inst.* 36 (2) (2017) 2633–2639, doi:10.1016/j.proci.2016.06.042.
- [11] F. Richecoeur, P. Scoufflaire, S. Ducruix, S. Candel, *J. Propuls. Power* 22 (4) (2006) 790–799, doi:10.2514/1.18539.
- [12] J.S. Hardi, S.K. Beinke, M. Oswald, B.B. Dally, *J. Propuls. Power* 30 (4) (2014) 991–1004, doi:10.2514/1.B35003.
- [13] T. Fiala, T. Sattelmayer, *Exp. Fluids* 56 (2015) 144, doi:10.1007/s00348-015-2013-8.
- [14] T. Fiala, T. Sattelmayer, S. Gröning, J. Hardi, R. Stützer, S. Webster, M. Oswald, *J. Propuls. Power* 33 (2) (2017) 490–500, doi:10.2514/1.B36280.
- [15] W. Armbruster, J.S. Hardi, D. Suslov, M. Oswald, *J. Propuls. Power* 35 (3) (2019) 632–644, doi:10.2514/1.B37406.
- [16] S. Gröning, J.S. Hardi, D. Suslov, M. Oswald, *J. Propuls. Power* 32 (3) (2016) 560–573, doi:10.2514/1.B35768.
- [17] A. Urbano, L. Selle, G. Staffelbach, B. Cuenot, T. Schmitt, S. Ducruix, S. Candel, *Combust. Flame* 169 (July 2016) 129–140, doi:10.1016/j.combustflame.2016.03.020.
- [18] J. Hardi, S. Gröning, S. Webster, S. Beinke, D. Suslov, M. Oswald, in: 52nd AIAA/ASME/SAE/ASEE Joint Propulsion Conference, AIAA Paper 2016–4893, Salt Lake City, UT, 2016, pp. 1–16, doi:10.2514/6.2016-4893.
- [19] S. Gröning, J.S. Hardi, D. Suslov, M. Oswald, *Progr. Propuls. Phys.* 11 (2019) 425–446, doi:10.1051/eucass/201911425.
- [20] S. Gröning, *Untersuchung selbsterregter Verbrennungsinstabilitäten in einer Raketenbrennkammer*, RWTH Aachen, Aachen, Germany, 2017 Ph.D. thesis.
- [21] R. Nez, T. Schmitt, M. Gonzalez-Flesca, S. Candel, S. Ducruix, in: 7th European Conference for Aeronautics and Aerospace Sciences (EU-CASS), Milan, Italy, 2017, pp. 1–15, doi:10.13009/EUCASS2017-369.